Systematic study of electronic states of Ln(O,F)BiS_2 by spin- and angle-resolved photoemission spectroscopy

Shi-Long Wu,[1] Koichiro Yaji,[2] Yuichi Ota,[3] Ayumi Harasawa,[3] Shik Shin,[3] Takehito Imai,[4,5] Koji Miyamoto,[4] Masanori Nagao,[6] Satoshi Watauchi,[6] Isao Tanaka,[6] Xiaoping Ma,[1] Huaixin Yang,[1] Yongqing Cai,[1] Lin Zhao,[1] Xingjiang Zhou,[1,*] and Taichi Okuda[4,†]

[1]*National Lab for Superconductivity, Beijing National Laboratory for Condensed Matter Physics, Institute of Physics, Chinese Academy of Sciences, Beijing 100190, China*

[2]*Research Center for Advanced Measurement and Characterization, National Institute for Materials Science, Ibaraki 305-0003, Japan*

[3]*Institute for Solid State Physics, University of Tokyo, Kashiwa, Chiba 277-8581, Japan*

[4]*Hiroshima Synchrotron Radiation Center, Hiroshima University, Higashi-Hiroshima 739-0046, Japan*

[5]*Graduate School of Science, Hiroshima University, Higashi-Hiroshima 739-8526, Japan*

[6]*Center for Crystal Science and Technology (CCST), University of Yamanashi, Yamanashi 400-8511, Japan*

(Received 29 April 2022; revised 23 August 2022; accepted 26 August 2022; published 20 September 2022)

The evolution of fine electronic structures in superconducting $LnO_{1-x}F_xBiS_2$ (Ln denotes lanthanoid) is systematically investigated with spin- and angle-resolved photoemission spectroscopy. A shape change of the Fermi surface (FS) at the X point from elliptical to rectangular with increasing the electron doping is commonly observed in different lanthanide systems. Besides that, an emergent large Fermi surface around the Γ point is also observed in all the samples with different doping levels deviating from the theoretical prediction, which might be related to the superconductivity. In addition, we found a humped band around $X(\pi,0)$ in the highly doped samples only, which may be attributed to the BiS_2 surface reconstruction or surface defects relying on the electron concentration. We also demonstrate the spin-selective excitation of photoelectrons, which indicates the presence of spin-orbital-entangled bulk Rashba splitting in this system. This result may enable the optical tuning of electron spin in a BiS_2-based system.

DOI: 10.1103/PhysRevB.106.104511

I. INTRODUCTION

Recently, $LnO_{1-x}F_xBiS(Se)_2$ (Ln = La/Ce/Pr/Nd) [1–5] was manifested as an unconventional superconductor with similar properties to those of cuprate superconductors, including a rather high value of $2\Delta/k_BT_C$ [6] and Cooper pairing symmetry [7,8]. The system exhibits a maximum superconducting critical temperature (T_C) of 10.6 K at $x \sim 0.5$ [1] among all the $BiS(Se)_2$-based superconductors. Furthermore, the so-called hidden Rashba effect with remarkable Rashba spin splitting with a magnitude of 100 meV was predicted in a $LaOBiS_2$ film. This effect is caused by strong polar fields between the buffer layer La_2O_2 and the BiS_2 layers, which sandwich the buffer layer [see Fig. 1(a)]. The pair of opposite polar fields causes the counterhelical Rashba spin polarization, which cancels each other and results in the hidden Rashba spin-split states [9,10]. According to Ref. [11], quite large Rashba splitting with the Rashba parameter $\alpha_R = 1.2$(eV Å) for the lowest conduction band (LCB) is observed in $LaO_{0.5}F_{0.5}BiS_2$.

Although such hidden Rashba spin-split states have been experimentally observed in some other two-dimensional (2D) materials [12–14] recently, the coexistence of hidden Rashba spin-split states and the superconductivity in bulk $LaO_{0.5}F_{0.5}BiS_2$ crystals [11] is quite unique, and it provides us with an interesting platform to investigate the interplay between its spin-polarized states and the superconductivity. In particular, all the previous SARPES studies of spin-polarized states in $LaO_{0.55}F_{0.45}BiS_2$ and cuprate Bi2212 [15] focused on their superconducting sheets; the buffer blocks were assumed to be an ignored effect for the layered local spin polarization. In this paper, we will inspect the plausible assumption by substituting the buffer blocks of a series of $LnO_{1-x}F_xBiS(Se)_2$ superconducting samples.

By the way, methods to enable electrically and/or optically tuning electronic states of strong spin-orbit coupling (SOC) are desired to artificially manipulate electron spins for a spin-field-effect transistor (spin-FET) [9,16] and spin-qubits [17,18]. According to previous experimental results [19,20], a linearly polarized light source can selectively excite spin-polarized electrons in several materials with strong SOC because of a dipole-matrix element effect, and that effect is termed "spin-selective excitation." Namely, spin-selective excitation in photoemission can be illustrated with the dipole transition term in the interaction Hamiltonian, taking both the mirror plane and the spin-orbital entanglement into account. So far, the surface electronic states with spin-orbital-entanglement in an elemental W (110) [19] and Bi

*XJZhou@iphy.ac.cn
†okudat@hiroshima-u.ac.jp

 ©2022 American Physical Society

TABLE I. Obtained $LnOBiS(Se)_2$ samples in our experiment.

		①–⑥:Grown in Yamanashi Univ. ⑦:Grown in Chinese Academy of Sciences			
Symbols	Samples	F doping level (nominal)	F doping level (by EDX)	F doping level (Luttinger theorem)	T_C (K) (ambient pressure)
①	$PrO_{0.87}F_{0.13}BiS_2$	0.20	0.13	0.178	2.4
②	$PrO_{0.77}F_{0.23}BiS_2$	0.40	0.23	0.280	4.0
③	$PrO_{0.74}F_{0.26}BiS_2$	0.60	0.26	0.291	4.3
④	$CeO_{0.73}F_{0.27}BiS_2$	0.44	0.27	0.162 [26]	3.1
⑤	$NdO_{0.71}F_{0.29}BiS_2$	0.30	0.29	0.241 [8]	5.1
⑥	$LaO_{0.55}F_{0.45}BiS_2$	0.50	0.45	0.215 [11]	3.2 (10.6 high pressure)
⑦	$LaO_{0.5}F_{0.5}BiSe_2$	0.55	0.50	0.220	3.3

(111) [20], a topological insulator Bi_2Se_3 [21–23], and a ternary alloy BiTeI [24,25], etc., were unveiled by previous experimental observations.

In spite of its clear interest, the possibilities of having spin-orbital entanglement in the $LnO_{1-x}F_xBiS_2$ system, namely its bulk Rashba spin polarization rotation with the linearly polarized lights, has not been investigated to date.

In this study, in order to reveal further the electronic states of the $LnO_{1-x}F_xBiS_2$ system, we performed high-resolution angle-resolved photoemission spectroscopy (ARPES) of a series of $LnO_{1-x}F_xBiS(Se)_2$ superconducting samples (see Table I) with the modulation of two different parameters, i.e., the electron-doping level and the lanthanide element. By utilizing the high-resolution ARPES system, the evolution of fermiology and its fine electronic structures are revealed. Furthermore, the spin-resolved lowest conduction band (LCB) and its spin-orbital entanglement are also revealed by laser-based SARPES with controlling the directions of an incident linearly polarized UV laser.

II. EXPERIMENTAL RESULTS AND DISCUSSIONS

As shown in Fig. 1(a), the crystal structure of $LnOBiS(Se)_2$ consists of triple-layer (TL) minimal blocks in which the LnO layer is sandwiched by BiS_2 layers. The TL blocks are stacked by a weak van der Waals force along the *c*-axis, and each block consists of a strong ionic bonding between a middle $(LnO)^+$ layer and two sandwiched $(BiS_2)^-$ layers. Namely, different lanthanide elements (Ln) bonding with oxygen have different electron affinities that significantly affect the strength of the ionic bond and also determine the fluorine-substitution level in oxygen sites. Thus, in the TL block, the $LnO_{1-x}F_x$ layer works as a reservoir of the electrons, and it applies a dipole field to the $BiS(Se)_2$ superconducting layers.

As shown in Table I, in our study seven types of superconducting compounds with different fluorine-doping levels from $x = 0.13$ in $PrO_{1-x}F_x$ block (sample ①) to $x = 0.5$ in $LaO_{1-x}F_x$ block (sample ⑦), which were determined by energy-dispersive x-ray spectroscopy (EDX) measurements, have been systematically observed. However, the doping level estimated by EDX measurement and from the Luttinger volumes of two-dimensional Fermi surface (FS) sheet enclosures obtained by ARPES measurement shows some deviation [see Fig. 2(c)]. In addition, the sample with different lanthanoid seems to have a different doping level, which may be due to the different electron affinity of lanthanoid atoms. Besides that, electrons could also be trapped on the cleaved surface because of the existence of Bi-S nano-zigzag chains with dangling bonds, which were first unveiled by recent STM/S measurements [27] as well as the possible defect states.

FS topology

We first observed the evolution of FS as a function of different doping levels and the lanthanide atoms. To precisely observe the entire FS, intensity mappings near the FS

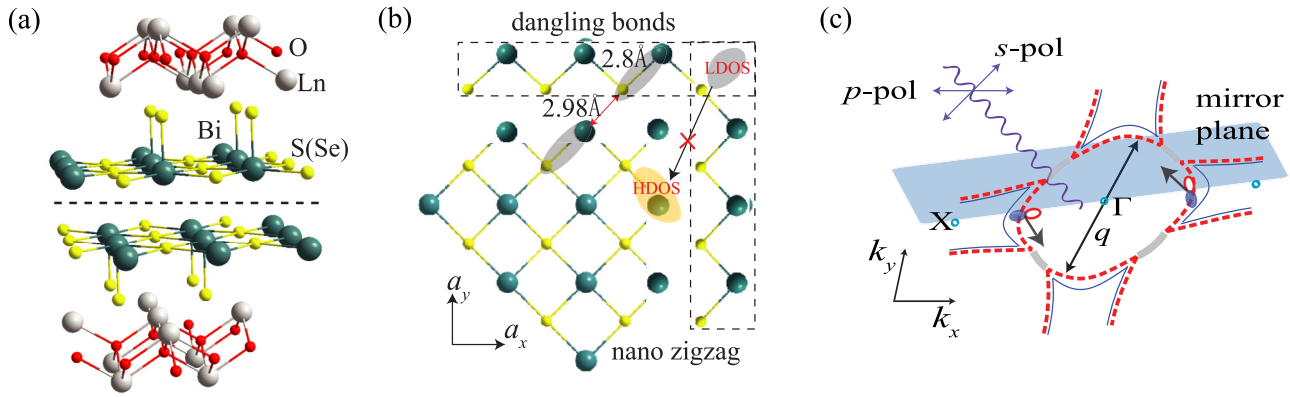

FIG. 1. (a) Crystal structure of $LnOBiS(Se)_2$. A black-dashed line denotes the position of the cleavage surface. (b) The top view of the BiS_2 surface. Two perpendicular nano-zigzag Bi-S chains, shown in a black-dashed box, reconstruct the BiS_2 surface and electronic structures. LDOS is defined as low density of states of Bi 6*p* electrons, and HDOS is defined as high density of states of Bi 6*p* electrons [27]. (c) Schematic diagrams of experimental geometries with reference to the spin-orbital-entangled Fermi surface of $LnO_{1-x}F_xBiS(Se)_2$.

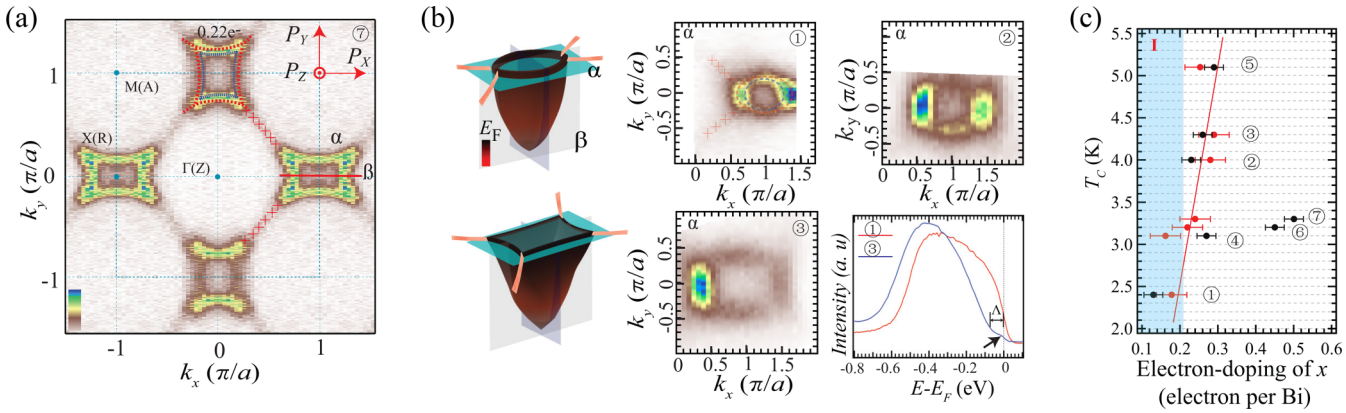

FIG. 2. (a) ARPES intensity mapping of the first Brillouin zone of $LaO_{0.5}F_{0.5}BiSe_2$ [number 7 in Fig. 1(a)], α branch electron pocket, and its spectra cutting line β. Coordinate axes (P_X, P_Y, P_Z) denote positive directions of spin vectors. (b) Comparative ARPES mapping of α branch electron-pocket in $PrO_{1-x}F_xBiS_2$ (numbers 1–3) and their energy dispersion curves (EDCs). "Λ" represents an opened band gap near FS. (c) T_C (left axis) vs electron-doping levels (bottom axis) of samples (①–⑦) (error-bar marks). Electron-doping levels are denoted with black marks corresponding to the energy-dispersive X-ray spectroscopy (EDX); the red marks represent the doping levels extracted from ARPES mappings of two-dimensional FS enclosures according to Luttinger' s theorem.

are integrated within ±20 meV above and below E_F. The high-resolution ARPES intensity mapping of $LaO_{0.5}F_{0.5}BiSe_2$ (sample ⑦) demonstrates that, as in Fig. 2(a), two small rectangular electronic Fermi pockets (indicated by red and blue dotted curves) around $X(\pi, 0)$ are observed.

Although it is hard to resolve the two pockets directly in the ARPES results, the SARPES measurement reveals that there are two pockets with opposite spin polarization [11]. The Fermi pockets enclose 8% and 14% of the Brillouin zone area, respectively, corresponding to an electron-doping level (x) of 0.22 per Bi site. The observed rectangular pockets around $X(\pi, 0)$ with fourfold symmetry are pretty consistent with theoretical anticipation at doping level $x = 0.25$ [28].

As shown in Fig. 2(b), in the sample with a smaller doping level (sample ①), smaller Fermi pockets with elliptic shape are observed. This elliptic Fermi pocket of sample ① with $x = 0.13$ changes to a larger Fermi pocket with increasing doping level (sample ②), and even the shape changes into a rectangular shape in the sample with $x = 0.26$ (sample ③). We observed FS pockets with different doping levels and lanthanoid atoms, and we estimated the electron-doping levels from the Luttinger volume of two-dimensional FS sheets. The relation between the estimated doping levels (red circles) as well as the doping level obtained by the EDX measurement (black circles) and the superconducting transition temperature (T_C) are summarized in Fig. 2(c).

As shown in Fig. 2(c), the doping levels obtained from the Luttinger volumes coincide more or less with their EDX values except for samples ⑥ and ⑦, which contain La atoms. The reason for this large deviation of the doping level by EDX in samples ⑥ and ⑦ is not clear at present. However, if we rely on the doping levels obtained by the Luttinger volume, the T_C values are linearly dependent on Luttinger volumes, i.e., the larger the electron-doping level, the higher T_C is. This result provides direct evidence that T_C is proportional to the actual electron-doping levels of the BiS_2 plane. As shown in Fig. 2(c), the lowest-doped sample (sample ①) with the elliptic Fermi pockets is still superconducting with the T_C of 2.4 K. The pretty small elliptic pockets of sample ① deviate remarkably from the theoretically expected [28] rectangular or large starlike pockets, which fulfill the condition of several nesting vectors between straight parts of Fermi pockets and could lead to both charge-density-wave (CDW) and higher superconducting transition (∼10.6 K). Our finding of the large deviation of doping level in samples ⑥ and ⑦ suggests that high T_C samples fabricated by the high-pressure technique [1] could benefit from an unrevealed mechanism by which doped electrons are smoothly transferred from $(LnO)^+$ layers to $(BiS_2)^-$ layers.

If one looks more closely at the FS in Fig. 2(a), however, there are some weakly bridged bands highlighted with red crosses in Fig. 2(a) connecting four isolated electronic pockets to form a holelike band around Γ(0,0) with a larger enclosure of the Brillouin zone, which is contrary to the aforementioned DFT calculations [28] at an $x = 0.25$ doping level since the weakly bridged spectra around the region would be located slightly above the Fermi level in the calculation. One could deduce that such a bridged band should only originate from the extension of band dispersion at the corner of the rectangular electron pockets of sample ③ ($x = 0.26$). However, as indicated in Fig. 2(b), the weakly bridged bands even appear at the corner of the elliptic electronic pocket of smaller doped samples with $x = 0.13$ (sample ①).

We can conclude and discuss the results by systematically investigating the evolution of FS with the actual doping level in superconducting $LnO_{1-x}F_xBiS_2$ (Ln denotes lanthanoid); we clarified the small Fermi pocket of elliptical shape which stems from a pretty low-doping superconducting sample ①. The shape change of Fermi pockets from elliptical to rectangular with increasing the electron doping is commonly observed in different lanthanide systems. Finally, a large FS around the Γ point connecting each rectangular Fermi pocket at the X point is also observed in all the samples with different doping levels deviating from the theoretical prediction, which might be related to the unconventional superconductivity [29–32].

$PrOBiS_2$ exhibits a mixed valence of Pr^{3+}/Pr^{4+}. The fluorine substitution cannot affect the ratio of Pr^{3+} to Pr^{4+}

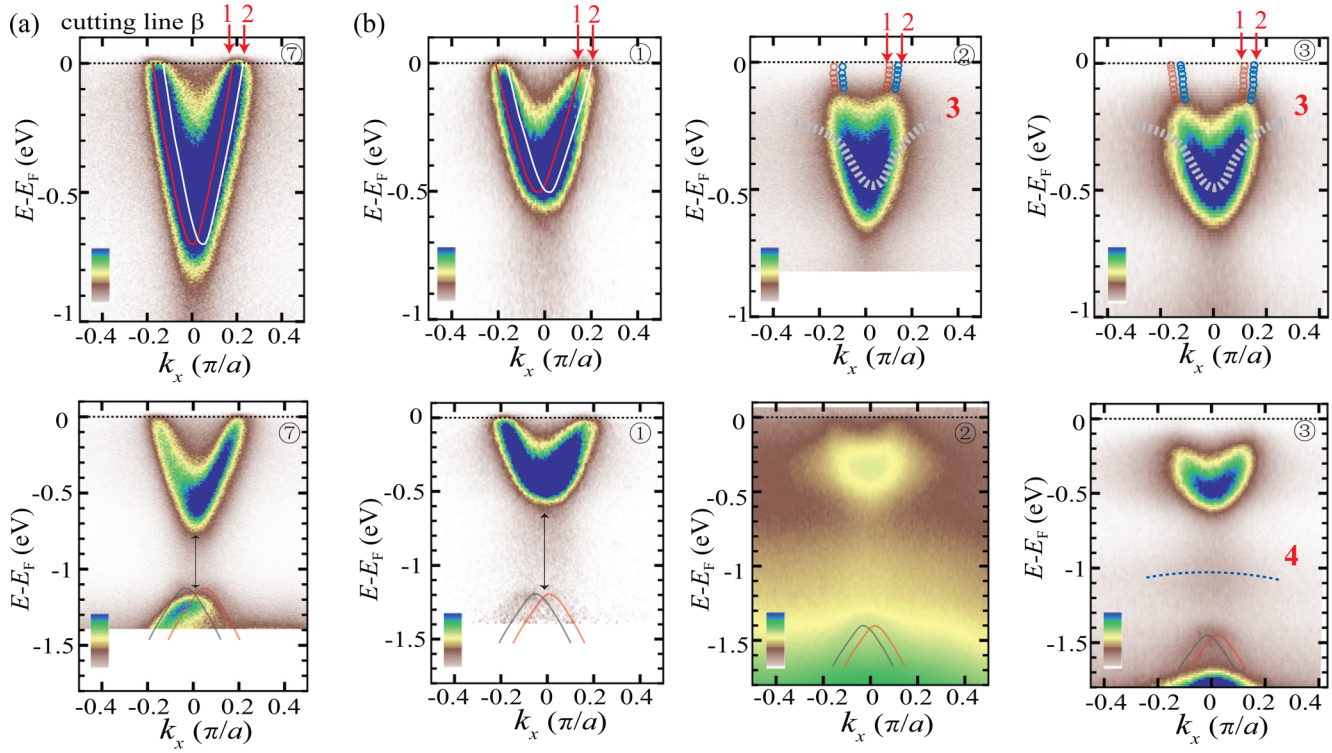

FIG. 3. (a) The bulk lowest conduction band (LCB) of sample ⑦ measured by ARPES ($h\nu = 21.2$ eV) along the cutting line β in Fig. 2(a); the arrows "1" and "2" denote two branches of a double-split band. (b) The bulk LCB branches along the cut β marked with numbers "1" and "2" as well as the undispersive states ("3") of samples ①–③ ($x = 0.13$, 0.23, and 0.26, respectively). A double arrow line denotes a band gap between the LCB and HVB. The flat in-gap band "4" is denoted with a dashed blue line.

[33–35], hence it provides an excellent superconducting platform with a homogeneous metallic state and tunable electron doping in BiS_2 sheets. The reshaping and classifying of two types of FS in the superconducting compounds are revealed by high-resolution ARPES experiments. Given that extra doped electrons come from the variable valency, the coexistence of the pretty small elliptic pockets at the X point and the large connected FS around the Γ point in the lowest doping sample ① might lead to an unclear mechanism by which doped electrons are dynamically transferred from $(PrO)^+$ layers to $(BiS_2)^-$ layers. Moreover, the deviation of doping level in samples ⑥ and ⑦ also suggests a possible variable valency of the sample Ln = La fabricated by the high-pressure technique, such that the dynamic transferring of electrons could become a dominant mechanism for reaching a higher T_C.

Fine electronic structures

To clarify the evolution of fine electronic states more precisely, we systematically investigated many samples with different doping levels. Figure 3(b) shows the EDCs near E_F of samples ①, ②, and ③ taken with a helium discharge lamp (21.22 eV). The obvious splitting of the lowest conduction band (LCB) was confirmed by the ARPES measurements (please also see Fig. S1 in the Supplemental Material) [11], as marked with arrows "1" and "2." These LCBs from 0 to 0.8 eV below the Fermi level are double-split bands caused by the hidden Rashba effect, as indicated in the previous SARPES measurement [11] and our present work [26] (see Fig. S1). The LCB is attributed mainly to the Bi $6p$ states. On the other hand, the bands near 1.2 eV are also Rashba-split bands [11], as indicated with red and blue curves, and they originate from $2p$ states of O and S atoms. Interestingly, although sample ① has strong ARPES spectral weights up to the Fermi level, those of samples ② and ③ shift down about 0.1–0.15 eV. The intensity of this band becomes relatively weak near the Fermi level in higher doping samples ② and ③. However, the band still crosses the Fermi level, as seen in the figures with increased contrast [see Fig. 3(b) below].

In addition to these previously reported bands, our ARPES data also indicate the presence of a faint humped band (marked "3"). As in Figs. 2(b) and 3(b), the humped bands present an energy gap of about $\Lambda \sim 0.1$ eV below E_F. In the larger energy range spectra in Fig. 3 (please also see the supplemental material, Fig. S2), in addition to the undispersive humped band ("3"), the in-gap flat band ("4") also appears when the electron-doping level is larger than 0.23.

Furthermore, it is shown by a double arrow line in Fig. 3 that the original energy gap of 0.6 eV between the topmost valence band and the bottom of the lowest conduction band of sample ① with $x = 0.13$ is enlarged to about 0.8 eV along with the band shifts in the higher doping samples (①0.13 < ②0.23 < ③0.26).

According to the density functional theory calculations of the BiS_2 plane [36], taking into account the soft phonon at the Brillouin zone $\Gamma(M)$ point, pioneered by Yildirim, sulfur atoms dynamically shift along the diagonal of the two-dimensional square in the BiS_2 plane and form two different Bi-S dangling bonds [bond lengths 2.80 and 2.98 Å, respectively, as shown in Fig. 1(b)], which make in-plane zigzag

Bi-S chains resulting in the reconstructed sheet. Additional experiments performed by utilizing scanning tunneling microscopy/spectroscopy (STM/S) [27] indicate an alternating arrangement of two types of dangling bonds on the BiS_2 cleavage surface, as schematically shown in Fig. 1(b). In addition, the STM measurement shows that the large number of disorders or defects appears in highly doped samples, causing the insulated electric conductivity in spite of the anticipated metallic/superconducting behaviors in the bulk materials, which may contribute to the newly appeared undispersive band ("3") and the in-gap flat band ("4"). On the other hand, the observed humped state and the indication of a lower density of states at the Fermi level may coincide with these previous observations in Nd(O,F)BiS_2 [37] and the sample $Na_{0.025}WO_3$ [38,39]. The disorder-induced self-trapping of polarons in $Na_{0.025}WO_3$ shows the temperature dependence of the spectral function. The conduction electrons are self-trapped due to strong disorders induced by the randomly distributed Na^+ ions, forming a weakly dispersive polaron band near the top of the valence bands, while a polaron decouples electrons at high temperature, which leads to a large decrease of the intensity of the humped state. These properties are quite similar to what we have observed in Pr(O,F)BiS_2 because we observed both spectral weights near the bottom of the conduction band (band "3") as well as the top of the valance band (band "4"). With consideration of the polaron model, the introduction of electron carriers by critical fluorine substitution that leads to more and more electrons flowing from $(PrO)^+$ buffer layers to the disordered $(BiS_2)^-$ surface might lead to a polaron state, by which an electron-level-dependent humped state could be properly explained. Furthermore, the previous DFT calculation [36] predicted that selenium substitution of the BiS_2 plane causes the formation of stable $BiSe_2$-based compounds by suppressing the local dynamic distortion in the BiS_2 plane [40]. Thus, the disappearance of the humped band "3" and band gap closing near E_F in Fig. 3(a) of the highly doped $BiSe_2$-based sample ⑦ are indirect evidences for the surface-disorder-induced polaron state [26].

Spin textures and spin-orbital-entangled bulk LCB

By utilizing the function of three-dimensional spin-vector analysis, the synchrotron radiation-based SR-SARPES measurements with linearly polarized photons were performed at 25 K (above T_C). The photon energy was set to 18 eV for the linear polarization. The experimental *p*- and *s*-polarization setups referring to the mirror plane are shown in Fig. 1(c). The CECs (constant energy contours) at E_F for the samples of different LnO-buffer layers are shown in Figs. 4(a), 4(c), and 4(e). For sample $PrO_{0.77}F_{0.23}BiS_2$, the rectangular shape possessing a larger enclosure of FS means that E_F is in close proximity to the Lifshitz transition as a consequence of the connected large FS around the Γ point. Both $PrO_{0.87}F_{0.13}BiS_2$ (sample ①) and $PrO_{0.77}F_{0.23}BiS_2$ (sample ②) possess the same helical spin textures for varied electron-doping levels as shown in Figs. 4(a) and 4(c).

Figures 4(b), 4(d), and 4(f) further show the spin-resolved intensities from positions "1" to "4" (the difference of spin-up and spin-down intensities) obtained by performing SR-SARPES measurements for $PrO_{0.87}F_{0.13}BiS_2$ and $PrO_{0.77}F_{0.23}BiS_2$ and $CeO_{0.73}F_{0.27}BiS_2$, respectively. The clear spin splitting of the conduction band can be observed for all the samples. As for the spin textures, those of FS were demonstrated in Figs. 4(a) and 4(c), helical spin textures of FS were experimentally observed in $PrO_{0.87}F_{0.13}BiS_2$ and $PrO_{0.77}F_{0.23}BiS_2$, while Figs. 4(b) and 4(d) show the spin-resolved EDCs in $PrO_{0.87}F_{0.13}BiS_2$ and $PrO_{0.77}F_{0.23}BiS_2$, respectively. The spin-resolved EDCs from positions "1" to "4" indicate that the peak shifting of the spin-up and spin-down intensities can be clearly observed with respect to the X point. As a result, spin intensity reversal occurs at peak positions, and the helical spin textures in $PrO_{1-x}F_xBiS_2$ are the same as that of $LaO_{0.55}F_{0.45}BiS_2$ [11] and $NdO_{0.71}F_{0.29}BiS_2$ [Fig. 5(c)]. However, spin-resolved EDCs at position "3" in Fig. 4(f) are evidently different from that in Figs. 4(b) and 4(d) since no spin intensity reversal occurs at two-peak positions. We can summarize the spin-resolved EDC results to schematically plot the nonhelical spin texture of circular FS in Fig. 4(e) for sample ④, which suggests a Dresselhaus-like nonhelical spin texture in $CeO_{0.73}F_{0.27}BiS_2$. The distinguished spin textures exist between Ce- and Pr- samples due to the LnO blocks between Ce(O, F)BiS_2 and Pr(O, F)BiS_2, which are associated with the polar interaction between the LnO and BiS_2 layers. The lattice constant c is $\sim$ 13.8 Å for Ln = Pr [41] and $\sim$ 13.6 Å for Ln = Ce [42], indicating that the separation between the BiS_2 layer and the LnO buffer layer decreases from Ln = Pr to Ln = Ce. Namely, Ce(O,F)BiS_2 could likely be considered a three-dimensional compound. Moreover, both Ce(O,F)BiS_2 and Pr(O,F)BiS_2 exhibit a mixed valence of Ce^{3+}/Ce^{4+} and Pr^{3+}/Pr^{4+}, respectively. In the Ce^{3+}/Ce^{4+} valence-variable state for Ln = Ce, the Ce $4f$ orbitals are hybridized with the Bi $6p$ orbitals via the S $3p$ orbitals at the out-of-plane sulfur site [35]. Since this hybridization channel is sensitive to the local displacement of the out-of-plane sulfur site, the system Ln = Ce tends to be inhomogeneous, which may create a Dresselhaus-like spin texture of FS.

Figure 5 shows the results of laser-SARPES measurements of the bulk lowest conduction band (LCB) with high-energy resolution and large electron-attenuation length for the sample ⑤ with $x = 0.29$ by utilizing the linearly polarized low-energy laser source of 6.994 eV. As in Fig. 5(a), the splitting of bulk LCB can be clearly revealed experimentally. That is, the Rashba-split LCB [bands "1" and "2" in Fig. 5(a)] can be observed, and its spin-resolved intensity mapping of P_Y in Fig. 5(b) (equal tangential spin to the FS) along the cutting line β unambiguously confirmed the spin polarization of the bulk band dispersion at the X point. The definitions of positive directions of spin vectors are shown with the coordinate axes (P_X, P_Y, P_Z) in Fig. 2(a). In Fig. 5(b), the experimental spin-resolved LCB dispersion on the left side is concatenated to the schematic illustration of full band dispersion (right side), which cannot be reached by experiment because of the low-energy laser source. The faint humped band "3" that is schematically shown in Fig. 3(b) is not observed in the high doping level sample, probably due to the bulk-sensitive measurement by the low-energy UV laser (6.994 eV) excitation instead of surface-sensitive measurement by a helium lamp (21.22 eV).

In Fig. 5(c), we demonstrated the spin-polarized energy distribution curves (EDCs) of P_Y for the LCB measured with

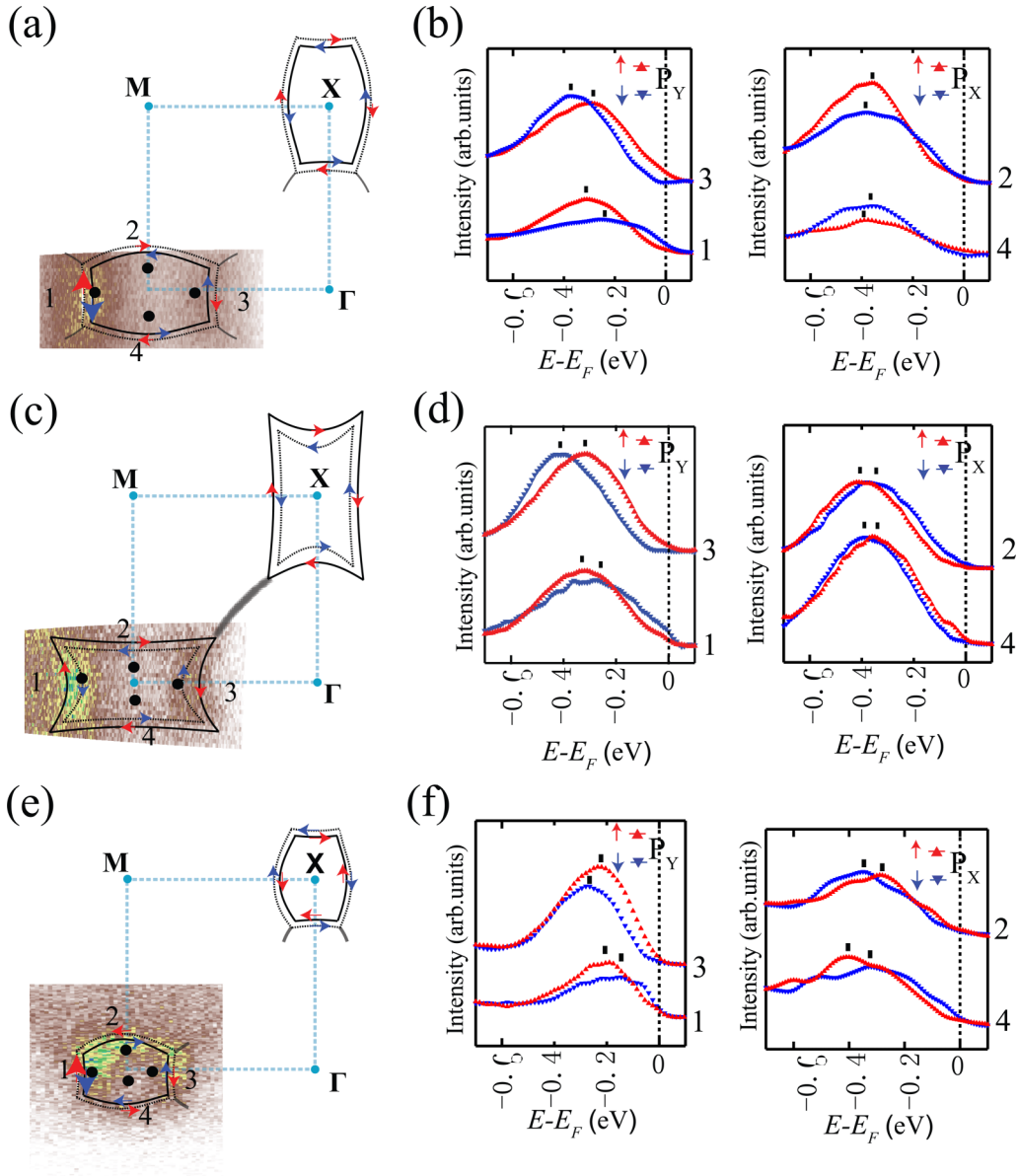

FIG. 4. Schematic diagrams of spin textures of FS and spin-resolved EDCs of $PrO_{0.87}F_{0.13}BiS_2$ (sample ①) and $PrO_{0.77}F_{0.23}BiS_2$ (sample ②) and $CeO_{0.73}F_{0.27}BiS_2$ (sample ④) by synchrotron radiation based (SR)-SARPES. (a), (c), and (e) SR-ARPES intensity mapping and schematic plotting of spin textures of FS of $PrO_{0.87}F_{0.13}BiS_2$ and $PrO_{0.77}F_{0.23}BiS_2$ and $CeO_{0.73}F_{0.27}BiS_2$. (b), (d), and (f) Spin-resolved EDCs around X at momentum points from "1" to "4" with p-polarized SR light of 18 eV photon energy, which is corresponding to $PrO_{0.87}F_{0.13}BiS_2$ and $PrO_{0.77}F_{0.23}BiS_2$ and $CeO_{0.73}F_{0.27}BiS_2$, respectively.

different light polarization. The electronic pockets along k_x and k_y have obvious orbital distinctions of Bi $6p_x$ and $6p_y$ orbitals, respectively. As shown in Fig. 1(c), by changing the polarization of the linearly polarized laser, the spin-resolved EDCs at the k_x point indicated with an arrow in Fig. 5(b) were measured with p- and s-polarized light. Because of the dipole matrix effect of photoemission, even (odd) initial states of a p_x (p_y) orbital referring to a mirror plane can be selectively observed by $p(s)$-polarized laser-SARPES observations. As shown in Fig. 5(c), the spin-resolved EDC taken with a p-polarized laser indicates opposite spin polarization to that taken with an s-polarized laser. The spin reversal of EDCs results from changing of the electric-field-vector direction of the linearly polarized laser from horizontal to vertical, manifesting the spin-orbital-entangled LCB. By referring to other SARPES results in the BiS_2-based familiar scenario (please see more spin-polarized EDCs of other lanthanoid-included samples from Fig. 4) in which the helical spin texture of the Fermi pocket around $X(\pi, 0)$ was revealed for Ln = La [11], Pr, and Nd samples by p-polarized synchrotron radiation, the spin-selective excitation changes the helical spin texture of a rectangular Fermi pocket into a counterhelical spin texture, as schematically shown in the inset of Fig. 5(c). By the selective excitation of the linearly combined even and odd states of the wave functions of LCB, the spin directions of photoelectrons can be readily reversed by tuning the linear polarization axis of the light even with the photon energy fixed. Because of the strong spin-orbit coupling, the spin-orbital entanglement

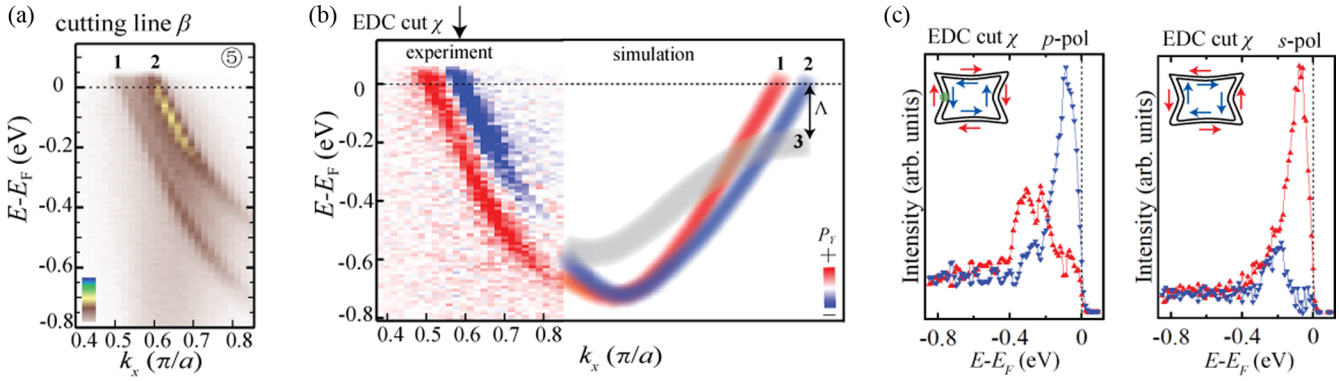

FIG. 5. (a) LCB of sample ($x = 0.29$, 5) along the cutting line β measured by ARPES with a p-polarized ultraviolet (UV) laser source of 6.994 eV photon energy [43]. (b) The concatenation of experimental spin-resolved LCB dispersion (left side) and theoretical simulation of LCB dispersion (bands "1" and "2" only; see the supplemental material) (right side). (c) Spin-resolved energy distribution curves (EDCs) at EDC cut χ taken with p- and s-polarized UV lasers, respectively.

can be generalized from the surface state to the bulk LCB in the $LnOBiS_2$ system, as demonstrated in Fig. 5(c). That is, our results illustrate that the bulk electrons of different orbital symmetries are selectively excited from the lowest conduction band dominated by spin-orbital entanglement. Thus, the spin-selective excitation of strong SOC bulk materials offers a platform for fabricating the photocathodes as a spin-polarized electron source with tunable spin directions. The disadvantage of commonly used GaAs photocathodes [44,45] as spin-polarized electron sources is that either tuning the directions of electron spin or fabricating the heterojunction film is more difficult than that in $LnO_{1-x}F_xBiS_2$ bulk materials, thus they could be exploited to fabricate an efficient photocathode.

III. CONCLUSIONS

In summary, we have systematically investigated the novel $BiS(Se)_2$-based superconductors with different lanthanides and doping levels by ARPES and spin-resolved ARPES. Small elliptic electronic pockets in the superconducting samples are identified in the low-doping samples, which is contrary to previous theoretical scenarios of nesting vectors between the larger starlike electronic pockets around $X(\pi,0)$. This finding will contribute to the further understanding of superconductivity in the $LnO_{1-x}F_xBiS_2$ system.

In addition, we have found a humped band and a flat band around $X(\pi, 0)$ in the samples above a critical electron-doping level which might come from the surface state or surface defects state. We also demonstrate that due to the presence of spin-orbital entanglement in the bulk conduction band around $X(\pi, 0)$, which exhibits different orbital symmetries (referred to as the aforementioned spin-selective excitation of photoelectrons), its bulk spin polarization is rotating with linearly polarized light. This finding offers us a pathway to manipulate the electron spin in bulk materials by adjusting the $s-(p-)$ polarized UV laser.

IV. METHODS

A. Crystal growth

$La(O,F)BiS_2$ single crystals were grown by a high-temperature flux method in a vacuumed quartz tube. The raw materials of La_2S_3, Bi, Bi_2S_3, Bi_2O_3, and BiF_3 were weighed to have a nominal composition of $LaO_{0.4}F_{0.6}BiS_2$. A mixture of raw materials (0.8 g) and CsCl/KCl flux (5.0 g) with a molar ratio of 5:3 was combined using a mortar and then sealed in a quartz tube under vacuum. The quartz tube was heated at 800 °C for 10 h, cooled slowly to 600 °C at a rate of 1 °C h^{-1}, and then furnace-cooled to room temperature. The quartz tube was opened to the air, and the flux was dissolved into distilled water in the tube. $LaO_{0.55}F_{0.45}BiS_2$ single crystals were obtained in this product. The obtained single crystals had good cleavages, producing flat surfaces as large as $\sim 1 \times 1\ mm^2$. The actual compositions of the examined samples were analyzed using energy-dispersive x-ray spectroscopy (EDX) on a TM-3030 instrument (Hitachi). The average value of x from EDX was calculated using the data obtained for five points on the sample surface.

B. Laser-(S)ARPES and synchrotron radiation (SR)-(S)ARPES measurements

Our laser-ARPES and laser-SARPES measurements using an ultraviolet laser were performed at the Institute for Solid State Physics, The University of Tokyo [43]. Our laser system provides 6.994-eV photons. Photoelectrons were analyzed with a combination of a ScientaOmicron DA30L analyzer and twin very-low-energy electron-diffraction (VLEED) -type spin detectors. The effective Sherman function was set to 0.27. The experimental geometry is represented in Fig. 1(c). The light incident plane is in the x-z plane on the sample axis, which corresponds to the mirror plane. We used linearly polarized light, and the direction of its electric-field vector is arbitrarily adjustable between the p- and s-polarizations. The energy and angular resolutions were set to 6 meV and 0.7 °, respectively. The sample temperature was kept at 25 K during the laser-(S)ARPES measurements. The spot size of the UV laser is 50 μm. A Scienta Omicron helium discharge lamp with photon energies of 21.2 and 40.8 eV was also used as the light source at Tokyo University. The energy resolution for He-ARPES was set to 20 meV. The energy resolution and the position of E_F were calibrated by the Fermi edge of a Cu block attached to the samples. The samples were cleaved *in situ* under ultrahigh vacuum (UHV) below 1×10^{-8} Pa.

An ESPRESSO machine for SR-ARPES and SR-SARPES measurements at Hiroshima University [46] can resolve both out-of-plane (P_Z) and in-plane (P_X /P_Y) spin polarization components with high angular and energy resolutions. The overall experimental energy and wave number resolutions of ARPES (SARPES) were set to 35 meV and < 0.008 Å^{-1} (60 meV and < 0.04 Å^{-1}), respectively. The samples were cleaved *in situ* under ultrahigh vacuum (UHV) below 1×10^{-8} Pa. The energy resolution and the position of E_F were calibrated by the Fermi edge of an Au film near the samples.

C. High-resolution ARPES measurements

High-resolution angle-resolved photoemission measurements for sample ⑦ were carried out on our lab-based system [47] that is equipped with a Scienta Omicron DA30L electron analyzer. A Scienta Omicron helium discharge lamp with photon energies of 21.2 and 40.8 eV was used as the light source. The energy resolution was set at 10 meV for FS mapping and band-structure measurements. The angular resolution was ~0.3°. Samples were measured at 25 K to avoid sample charging. All measurements were carried out in ultrahigh vacuum with a base pressure better than 6.7×10^{-9} Pa.

ACKNOWLEDGMENTS

The authors would like to thank Z. X. Liu, X. Y. Hou, and C. Zhang for helpful discussion. This paper is primarily supported by the BL-9B endstation, Hiroshima Sychrotron Radiation Center (HiSOR Proposal No. 16AG052). We also acknowledge the ISSP, University of Tokyo, for provision of laser beamtime, and we would like to gratefully acknowledge China Postdoctoral Science Foundation Grant (Grant No. E0BK141).

S.W., K.Y., Y.O., A.H., K.M., T.I., Y.C., L.Z., and T.O. carried out ARPES and SARPES measurement. M.N., S.W., I.T., X.M., and H.Y. synthesized and characterized the single crystals. S.W. analyzed (S)ARPES data and wrote the manuscript with input from X.Z., S.S., and T.O. S.W. and T.O. conceived the experiment. All authors contributed to the scientific discussions.

[1] Y. Mizuguchi, S. Demura, K. Deguchi, Y. Takano, H. Fujihisa, Y. Gotoh, H. Izawa, and O. Miura, J. Phys. Soc. Jpn. **81**, 114725 (2012).
[2] J. Xing, S. Li, X. X. Ding, H. Yang, and H. H. Wen, Phys. Rev. B **86**, 214518 (2012).
[3] R. Jha, A. Kumar, S. K. Singh, and V. P. S. Awana, J. Supercond. Nov. Magn. **26**, 499 (2013).
[4] R. Jha, A. Kumar, S. Kumar Singh, and A. V. P. S. Awana, J. Appl. Phys. **113**, 056102 (2013).
[5] S. Demura, Y. Mizuguchi, K. Deguchi, H. Okazaki, H. Hara, T. Watanabe, S. James Denholme, M. Fujioka, T. Ozaki, H. Fujihisa, and Y. Gotoh, J. Phys. Soc. Jpn. **82**, 033708 (2013).
[6] J. Liu, D. Fang, Z. Wang, J. Xing, Z. Du, S. Li, X. Zhu, H. Yang, and H. H. Wen, Europhys. Lett. **106**, 67002 (2014).
[7] T. Agatsuma and T. Hotta, J. Magn. Magn. Mater. **400**, 73 (2016).
[8] Y. Ota, K. Okazaki, H. Q. Yamamoto, T. Yamamoto, S. Watanabe, C. Chen, M. Nagao, S. Watauchi, I. Tanaka, Y. Takano, and S. Shin, Phys. Rev. Lett. **118**, 167002 (2017).
[9] Q. Liu, Y. Guo, and A. J. Freeman, Nano Lett. **13**, 5264 (2013).
[10] X. Zhang, Q. Liu, J. W. Luo, A. J. Freeman, and A. Zunger, Nat. Phys. **10**, 387 (2014).
[11] S. -L. Wu, K. Sumida, K. Miyamoto, K. Taguchi, T. Yoshikawa, A. Kimura, Y. Ueda, M. Arita, M. Nagao, S. Watauchi, I. Tanaka, and T. Okuda, Nat. Commun. **8**, 1919 (2017).
[12] A. M. Jones, H. Yu, J. S. Ross, P. Klement, N. J. Ghimire, J. Yan, D. G. Mandrus, W. Yao, and X. Xu, Nat. Phys. **10**, 130 (2014).
[13] J. M. Riley, F. Mazzola, M. Dendzik, M. Michiardi, T. Takayama, L. Bawden, C. Granerød, M. Leandersson, T. Balasubramanian, M. Hoesch, T. K. Kim, H. Takagi, W. Meevasana, Ph. Hofmann, M. S. Bahramy, J. W. Wells, and P. D. King, Nat. Phys. **10**, 835 (2014).
[14] K. Zhang, S. Zhao, Z. Hao, S. Kumar, E. F. Schwier, Y. Zhang, H. Sun, Y. Wang, Y. Hao, X. Ma, C. Liu, L. Wang, X. Wang, K. Miyamoto, T. Okuda, C. Liu, J. Mei, K. Shimada, C. Chen, and Q. Liu, Phys. Rev. Lett. **127**, 126402 (2021).
[15] K. Gotlieb, C-Y. Lin, M. Serbyn, W. Zhang, C. L. Smallwood, C. Jozwiak, H. Eisaki, Z. Hussain, A. Vishwanath, and A. Lanzara, Science **362**, 1271 (2018).
[16] S. Datta and B. Das, Appl. Phys. Lett. **56**, 665 (1990).
[17] T. Kobayashi, J. Salfi, C. Chua, J. van der Heijden, M. G. House, D. Culcer, W. D. Hutchison, B. C. Johnson, J. C. McCallum, H. Riemann, and N. V. Abrosimov, Nat. Mater. **20**, 38 (2020).
[18] K. D. Petersson, L. W. McFaul, M. D. Schroer, M. Jung, J. M. Taylor, A. A. Houck, and J. R. Petta, Nature (London) **490**, 380 (2012).
[19] K. Miyamoto, H. Wortelen, T. Okuda, J. Henk, and M. Donath, Sci. Rep. **8**, 10440 (2018).
[20] K. Yaji, K. Kuroda, S. Toyohisa, A. Harasawa, Y. Ishida, S. Watanabe, C. Chen, K. Kobayashi, F. Komori, and S. Shin, Nat. Commun. **8**, 14588 (2017).
[21] O. V. Yazyev, J. E. Moore, and S. G. Louie, Phys. Rev. Lett. **105**, 266806 (2010).
[22] Y. Cao, J. A. Waugh, X. W. Zhang, J. W. Luo, Q. Wang, T. J. Reber, S. K. Mo, Z. Xu, A. Yang, and J. Schneeloch, Nat. Phys. **9**, 499 (2013).
[23] Z. Xie, S. He, C. Chen, Y. Feng, H. Yi, A. Liang, L. Zhao, D. Mou, J. He, Y. Peng, X. Liu, Y. Liu, G. Liu, X. Dong, L. Yu, J. Zhang, S. Zhang, Z. Wang, F. Zhang, F. Yang, Q. Peng, X. Wang, C. Chen, Z. Xu, and X. J. Zhou, Nat. Commun. **5**, 3382 (2014).
[24] L. Bawden, J. M. Riley, C. H. Kim, R. Sankar, E. J. Monkman, D. E. Shai, H. I. Wei, E. B. Lochocki, J. W. Wells, W. Meevasana, and T. K. Kim, Sci. Adv. **1**, e1500495 (2015).
[25] H. Maaß, H. Bentmann, C. Seibel, C. Tusche, S. V. Eremeev, T. R. Peixoto, O. E. Tereshchenko, K. A. Kokh, E. V. Chulkov, J. Kirschner, and F. Reinert, Nat. Commun. **7**, 11621 (2016).
[26] See Supplemental Material at http://link.aps.org/supplemental/10.1103/PhysRevB.106.104511 for additional information.
[27] T. Machida, Y. Fujisawa, M. Nagao, S. Demura, K. Deguchi, Y. Mizuguchi, Y. Takano, and H. Sakata, J. Phys. Soc. Jpn. **83**, 113701 (2014).

[28] H. Usui, K. Suzuki, and K. Kuroki, Phys. Rev. B **86**, 220501(R) (2012).
[29] H. Kotegawa, Y. Tomita, H. Tou, H. Izawa, Y. Mizuguchi, O. Miura, S. Demura, K. Deguchi, and Y. Takano, J. Phys. Soc. Jpn. **81**, 103702 (2012).
[30] X. Wan, H.-C. Ding, S. Y. Savrasov, and C.-G. Duan, Phys. Rev. B **87**, 115124 (2013).
[31] C. Morice, E. Artacho, S. E. Dutton, H. -J. Kim, and S. S. Saxena, J. Phys. Condens. Matter **28**, 345504 (2016).
[32] S. Cobo-Lopez, M. S. Bahramy, R. Arita, A. Akbari, and I. Eremin, New. J. Phys. **20**, 043029 (2018).
[33] S. Ishii, Y. Hongu, A. Miura, and M. Nagao, Appl. Phys. Express **9**, 063101 (2016).
[34] S. Dash, T. Morita, K. Kurokawa, Y. Matsuzawa, N. L. Saini, N. Yamamoto, J. Kajitani, R. Higashinaka, T. D. Matsuda, Y. Aoki, and T. Mizokawa, Phys. Rev. B **98**, 144501 (2018).
[35] T. Sugimoto, B. Joseph, E. Paris, A. Iadecola, T. Mizokawa, S. Demura, Y. Mizuguchi, Y. Takano, and N. L. Saini, Phys. Rev. B **89**, 201117(R) (2014).
[36] T. Yildirim, Phys. Rev. B **87**, 020506(R) (2013).
[37] L. K. Zeng, X. B. Wang, J. Ma, P. Richard, S. M. Nie, H. M. Weng, N. L. Wang, Z. Wang, T. Qian, and H. Ding, Phys. Rev. B **90**, 054512 (2014).
[38] S. Raj, D. Hashimoto, H. Matsui, S. Souma, T. Sato, T. Takahashi, D. D. Sarma, P. Mahadevan, and S. Oishi, Phys. Rev. Lett. **96**, 147603 (2006).
[39] S. Raj, T. Sato, S. Souma, T. Takahashi, D. D. Sarma, and P. Mahadevan, Mod. Phys. Lett. B **23**, 2819 (2009).
[40] Q. Liu, X. Zhang, and A. Zunger, Phys. Rev. B **93**, 174119 (2016).
[41] M. Nagao, A. Miura, R. Matsumoto, S. Watauchi, Y. Takano, and I. Tanaka, Solid State Commun. **296**, 17 (2019).
[42] R. Higashinaka, T. Asano, T. Nakashima, K. Fushiya, Y. Mizuguchi, O. Miura, T. D. Matsuda, and Y. Aoki, J. Phys. Soc. Jpn. **84**, 023702 (2015).
[43] K. Yaji, A. Harasawa, K. Kuroda, S. Toyohisa, M. Nakayama,Y. Ishida, A. Fukushima, S. Watanabe, C. Chen, F. Komori, and S. Shin, Rev. Sci. Instrum. **87**, 053111 (2016).
[44] D. T. Pierce and F. Meier, Phys. Rev. B **13**, 5484 (1976).
[45] C. Feng, Y. Zhang, Y. Qian, B. Chang, F. Shi, G. Jiao, and J. Zou, Opt. Express **23**, 19478 (2015).
[46] T. Okuda, K. Miyamaoto, H. Miyahara, K. Kuroda, A. Kimura, H. Namatame, and M. Taniguchi, Rev. Sci. Instrum. **82**, 103302 (2011).
[47] G. Liu, G. Wang, Y. Zhu, H. Zhang, G. Zhang, X. Wang, Y. Zhou, W. Zhang, H. Liu, L. Zhao, J. Meng *et al.*, Rev. Sci. Instrum. **79**, 023105. (2008).